Multifrequency and Multiload MCR-WPT System Based on Hysteresis Current Control

Anran Sun, Chenyang Xia, *Member, IEEE*, Yuhang Chen, Yunhai Liu, Ziyue Yang, Shuze Zhao, and Zijian Yang

***Abstract*—Aiming at the problems that existing multifrequency and multiload (MFML) magnetic coupling resonant wireless power transfer (MCR-WPT) systems either the output power frequencies are limited or a large amount of reactive power in them leads to decreased power factor (PF). This article proposes an MFML MCR-WPT system based on hysteresis current control, which controls multifrequency current superposition output and has equivalent current source characteristics. The system outputs multifrequency current by tracking the command current, which consists of subcommand currents designed according to load frequency and power requirements and raises PF without affecting power transfer quality by adding power compensating capacitor (C_{P}) with lower cost and design complexity than existing technologies. First, the system structure and working principle are introduced. Then, the criterion of equivalent current source is deduced, based on which the system model is established, and its characteristics are analyzed. After that, the system parameter design methods are given. Finally, an experimental platform is built to verify the proposed theory. The simulation and experimental results show that the proposed system can output multifrequency power, switch the frequency freely, and raise PF by adding *C*p without affecting power transfer.**

***Index Terms*—Hysteresis current (HC) control, magnetic coupling resonant wireless power transfer (MCR-WPT), multifrequency, multiload.**

I. Introduction

MAGNETIC coupling resonant wireless power transfer (MCR-WPT) technology is a kind of technology that transfers power without direct connection of wires. Compared with traditional wired transfer mode, it is more flexible and convenient [1]. At present, this technology has been gradually applied to numerical control robot [2], aerospace equipment [3], marine engineering equipment [4], advanced rail transit [5], new energy vehicles [6], biomedicine and precision medical instruments [7], and other fields, and has a huge application demand in the future.

With the progress of MCR-WPT technology, the research and application of its working mode have gradually expanded to multifrequency multiload (MFML) transfer mode [8], [9]. Compared with the existing single-frequency and single-load MCR-WPT system, the MFML MCR-WPT system mainly has the following characteristics: on the one hand, due to the inconsistent development of the WPT system standards, the operating frequencies of each load may be different. On the other hand, since the application scenarios and requirements of loads may be different, the power level of each load may be inconsistent. Therefore, to further promote the development of MCR-WPT technology, the research of MFML MCR-WPT system has been paid more and more attention by researchers.

According to the research on the transmission mode of the existing MFML MCR-WPT system, it can be mainly classified into multiple-inverter parallel operation technology [10], [11] and single-inverter operation technology [12], [13], [14], [15], [16], [17], [18], [19]. For multiple-inverter parallel operation technology, several inverters are used on the primary side, and the operating frequency of each inverter is different. Although this technology can be more convenient to generate and control power of different frequencies, but the structure of emitter is complex, which is difficult to miniaturize and make practical. However, compared with multiple-inverter parallel operation technology, single-inverter operation technology can output multifrequency power by a single inverter, which is easy to miniaturize and practicality of the system, so it has gradually become a research hotspot of MFML MCR-WPT technology.

The existing single-inverter operation technology can be mainly classified into fundamental-harmonic reuse technology [12], [13], [14], multifrequency power time-sharing technology [15], and multifrequency power superposition technology [16], [17], [18], [19].

1) For the fundamental-harmonic reuse technology, the fundamental wave and its harmonic components can be selectively used to achieve multifrequency power transfer. In [12], the fundamental component of the inverter output voltage is used for power transfer, and the third harmonic is used as the carrier of the signal to transmit the signal, which realizes the synchronous wireless transfer of power and signal. In [13], by Fourier decomposition of the output voltage of the inverter, the switching time

Manuscript received 26 September 2023; revised 26 January 2024; accepted 20 April 2024. Date of publication 24 April 2024; date of current version 20 June 2024. This work was supported in part by the National Natural Science Foundation of China under Grant 52277020, in part by the Natural Science Foundation of Jiangsu Province under Grant BK20211246, in part by the Postgraduate Research & Practice Innovation Program of Jiangsu Province under Grant KYCX23_2693, and in part by the Graduate Innovation Program of China University of Mining and Technology under Grant 2023WLKXJ192. Recommended for publication by Associate Editor C. Fernandez. *(Corresponding author: Chenyang Xia.)*

The authors are with the School of Electrical Engineering, China University of Mining and Technology, Xuzhou 221116, China (e-mail: sunar@cumt.edu.cn; chyxia@cumt.edu.cn; chen_yuhang@cumt.edu.cn; liuyunhai@cumt.edu.cn; yang.ziyue@cumt.edu.cn; tb20130011b3ld@cumt.edu.cn; yangzijian@cumt.edu.cn).

Color versions of one or more figures in this article are available at https://doi.org/10.1109/TPEL.2024.3393003.

Digital Object Identifier 10.1109/TPEL.2024.3393003

corresponding to the required frequency component is selected as the inverter switching signal to output fundamental wave and specific harmonics. In [14], a multifrequency power modulation method based on cosine switch frequency modulation technology is proposed to extend harmonic spectrum, which increases the number of power frequencies that can be outputted. Although this technology can make full use of the output voltage of inverter, it can only realize the power transfer of specific frequency, and there is an inherent coupling relationship between output power, which is difficult to achieve flexible adjustment of power.

2) For the multifrequency power time-sharing technology, multifrequency power is outputted in different time. In [15], three loads are charged at different time by switching the operating frequency of the inverter. However, this technology can only output power with a single frequency at the same time, and cannot realize the synchronous power supply of each load.
3) For the multifrequency power superposition technology, it outputs multifrequency power by changing the inverter control strategy. In [16], [17], and [18], the hybrid modulation waves sinusoidal pulse width modulation (HMW-SPWM) strategy is used to form composite modulated waves by superimposing multiple modulated waves of different frequencies and then outputs multifrequency power by modulating the composite modulated wave. In [19], the two bridge arms of the inverter run at different frequencies respectively, which uses a single inverter to output dual-frequency power.

Compared to the other single-inverter operation technologies, the multifrequency power superposition technology has the characteristics of simple structure and flexible control between different frequencies of power, which has attracted the attention of more researchers. However, the existing MFML MCR-WPT technologies output multifrequency power by controlling the voltage of different frequencies to be superimposed, which needs multifrequency resonance compensation (MFRC) network to achieve a better transfer effect. However, with the increase in the number of load frequencies, the order of the MFRC network will also increase [20], which not only increases the system volume but also greatly increases the design complexity. If the zero-compensation strategy is adopted, there will be a large amount of reactive power in the system, which will decrease the system power factor (PF).

To solve the abovementioned problems in existing MFML MCR-WPT systems, an MFML MCR-WPT system based on hysteresis current (HC) control is proposed in this article, which outputs multifrequency power by controlling the superposition of currents at different frequencies. This system has the equivalent current source characteristic that the existing control voltage superposition systems do not have, which makes the external circuit structure of the system only affect the overall power level but not affect the frequency component of the output current. The system can output multifrequency power steadily and switch the power frequency freely, and at the same time, it can raise PF by adding power compensating capacitance (C_{P}). Compared with the method of using the MFRC network, the use of C_{P} has lower cost and design complexity, and it does not need to add new circuit structure with the increase of the number of load frequencies, and the design complexity will not increase greatly. First, the corresponding subcommand current is designed according to the power and frequency requirements of each load, and the subcommand currents are superimposed to form the command current. Then the primary side current tracks the command current based on HC control to output multifrequency power. If the load requirements change, the corresponding subcommand current can be adjusted to meet the changed requirements. Since the output current of the system based on HC control is only controlled by the command current, it has the characteristics of the equivalent current source. Therefore, C_{P} can be added to the primary side to raise PF without affecting the frequency component of the output power, which greatly reduces the design complexity and cost of the system.

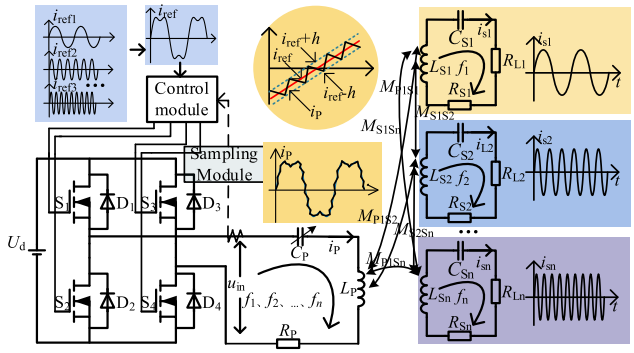

Fig. 1. Structure diagram of MFML MCR-WPT system based on HC control.

The rest of this article is organized as follows. In Section II, the structure and working principle of the MFML MCR-WPT system based on HC control are introduced. In Section III, the criterion of equivalent current source based on HC control is deduced, and then the system model is established and its characteristics are analyzed. Section IV introduces the system parameter design methods. In Section V, the experimental platform is set up to verify the characteristics of the system. Finally, Section VI concludes this article.

II. Structure and Working Principle of MFML MCR-WPT System Based on HC Control

A. System Structure

The structure of the MFML MCR-WPT system based on HC control proposed in this article is shown in Fig. 1.

As shown in Fig. 1, the primary side of the system adopts a single inverter structure, U_{d} is the dc source, L_{P} is the inductance of the transmitting coil, $R_{L\mathrm{P}}$ is the equivalent internal resistance of L_{P}, and C_{P} is the power compensation capacitance. The HC control module is set on the primary side of the system. The secondary side of the system has n receiving circuits (n is the number of loads at different operating frequencies). $M_{\mathrm{P1S}i}$ is the mutual inductance between the transmitting coil and i ($i = 1, 2, \ldots, n$) receiving coil, and $M_{\mathrm{S}i\mathrm{S}j}$ is the cross mutual inductance

between i receiving coil and j ($j = 1, 2, \ldots, n.\ i \neq j$) receiving coil. L_{Si} is the inductance of the i receiving coil. C_{Si} is the resonant capacitance, R_{Lsi} is the equivalent internal resistance of L_{Si}, and R_{Li} is the load equivalent internal resistance. C_{Si} and L_{Si} form an S-type resonant network, satisfying the relationship as follows:

$$(2\pi f_i)^2 L_{Si} C_{Si} = 1 \tag{1}$$

where f_i is the operating frequency of the i pick-up circuit.

Compared with the multi-inverter topology, the proposed topology can realize the parallel output and decoupling control of multifrequency power with fewer devices. It can meet the application requirements of parallel power supply for different frequency loads.

B. System Working Principle

The HC control is a closed-loop control method, which has the characteristics of simple hardware circuits and fast circuit response. The basic control principle is as follows: the expected output current waveform is taken as the command current, the actual current is taken as the feedback signal, and the instantaneous value is compared to determine the ON-OFF of the power switch device of the inverter circuit, so that the actual output current tracks the command current within the hysteresis width h.

In the MFML MCR-WPT system, since the power and frequency levels of each load are different, and the corresponding subcommand current is designed according to the requirement of each load. All the subcommand currents are superimposed to form a command current. By tracking the command current within h, the multifrequency current required by the loads is outputted. The command current is as follows:

$$i_{\text{ref}} = \sum_{i=1}^{n} i_{\text{ref}i} = \sum_{i=1}^{n} a_i \sin(2\pi f_i t + \varphi_i) \tag{2}$$

where $i_{\text{ref}i}$ ($i = 1, 2, \ldots, n$) is the subcommand current, which includes frequency parameter f_i, amplitude parameter a_i, and phase parameter φ_i.

Fig. 2(a) shows the dual-frequency command current and its corresponding subcommand current frequency components. The i_{ref} has the characteristics of each subcommand current at the same time. Fig. 2(b) shows the simulation waveform of the output current and voltage of the inverter based on HC control. As we can see the output current i_{P} tracks i_{ref} within h, and the output voltage u_{in} frequency is not fixed.

The system based on HC control has the characteristic that the main frequency component of i_{P} is only affected by i_{ref}. Therefore, the output of multifrequency current can be realized by tracking i_{ref}, which consists of subcommand currents at different frequencies. At the same time, adding C_{P} will only affect the overall reactive power of the system, but will not affect the main frequency component of i_{P}. Hence, the MFML MCR-WPT system based on HC control can output multifrequency current and raise PF by adding C_{P}.

The secondary side pick-up circuits use a series resonance network. Due to the different operating frequencies of each pick-up circuit, there is a certain frequency isolation effect between pick-up circuits. In addition, the circuit quality factor is raised as much as possible in the process of parameter design, to ensure that the interference conditions of power between different pick-up circuits are met, and multifrequency power decoupling transfer is realized [18].

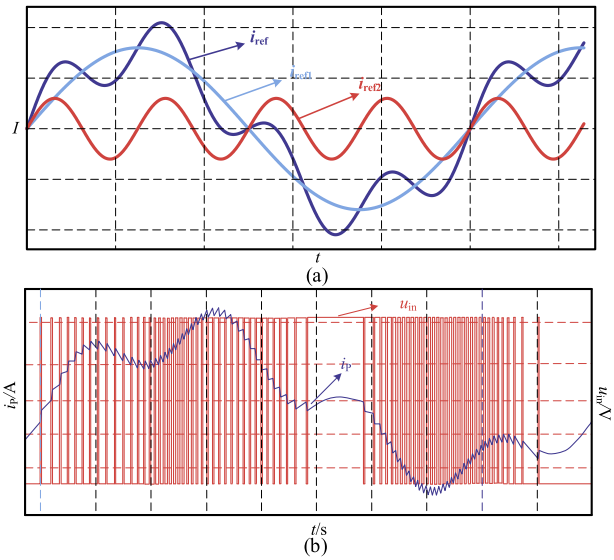

Fig. 2. i_{ref} and corresponding i_{P} and u_{in} simulation waveform. (a) i_{ref} and the frequency components it contains. (b) i_{P} and u_{in} simulation waveform.

To sum up, the characteristics of the MFML MCR-WPT system based on HC control are as follows.

1) The system controls the current superposition based on HC control to output multifrequency power. When the equivalent current source criterion is met, system has the characteristic of the equivalent current source, which allows the external circuit structure of the system to affect only the overall power level but not the frequency component of the output current.
2) Each subcommand current corresponds to a load, and there is no coupling relationship between subcommand currents, which can realize flexible decoupling control between the power of different frequencies.
3) Due to the equivalent current source characteristic, the system can raise PF without affecting the main frequency components of i_{P} by adding C_{P} in a way with lower cost and design complexity than existing technologies.

III. System Model Analysis

It can be seen from Section II that the output current of MFML MCR-WPT system based on HC control is only controlled by i_{ref} and does not change with the parameters of the external circuit, so the inverter can be equivalent to the current source whose output is i_{ref}. However, the equivalent current source characteristics of the system must be established conditionally. In this section, the criterion that the inverter can be modeled as an equivalent current source is deduced, and then the system model is modeled based on this criterion, and its characteristics are analyzed.

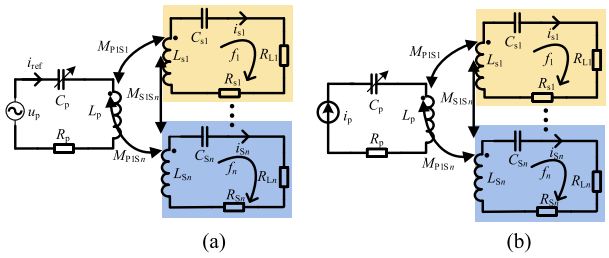

Fig. 3. Equivalent models of MFML MCR-WPT system. (a) System model based on the voltage source. (b) System model based on the equivalent current source.

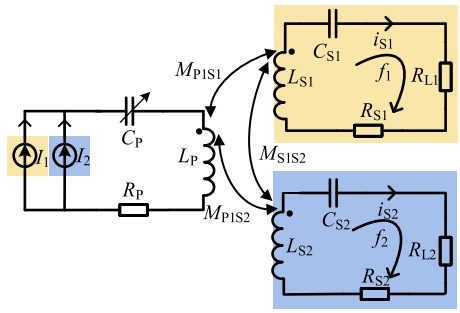

Fig. 4. Equivalent model of dual-frequency dual-load MCR-WPT system.

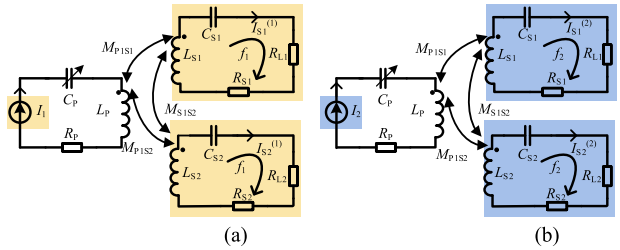

Fig. 5. Equivalent circuits at different operating frequencies. (a) I_1 in acting alone. (b) I_2 in acting alone.

A. Modeling Criteria for Equivalent Current Source

According to Section II, the output current of the system based on HC control tracks the i_{ref} within h. The output current of the inverter is completely controlled by i_{ref}, the frequency of the output voltage changes constantly with i_{ref}, and the change of circuit parameters does not affect the frequency component of the output current. When h is set reasonably, the output current can be equivalent to i_{ref}. This HC-controlled inverter output characteristic is completely different from other technologies where the output voltage is fixed and the output current changes with the current circuit impedance. However, the output current of the inverter is different from the standard current source type inverter circuit, it only has the equivalent current source characteristic that the output current of inverter is independent of the impedance angle of the external circuit.

Therefore, under the condition that the i_{p} can track the i_{ref}, the main frequency component of i_{p} is only controlled by i_{ref} and is independent of the external circuit structure, which conforms to the current source characteristics [21], [22]. So, the inverter model can be transformed from the voltage source to the current source whose output is i_{p}. The system models based on voltage source and equivalent current source are shown in Fig. 3.

If the i_{P} is outputted according to i_{ref}, i_{P} is a multifrequency hybrid equivalent current source, the u_{P} is an ideal voltage source superimposed by the frequency components contained in the i_{ref}. The expression of i_{P} is shown in the following equation:

$$i_{\mathrm{P}} = i_{\mathrm{ref}} = i_{\mathrm{P1}} + i_{\mathrm{P2}} + \cdots + i_{\mathrm{P}n} = \sum_{i=1}^{n} a_i \sin(2\pi f_i t + \varphi_i). \tag{3}$$

According to Fig. 3(a), the KVL formula for the primary side circuit is written as shown in (4) and (5)

$$u_{\mathrm{p}} = u_{C_{\mathrm{P}}} + u_{L_{\mathrm{P}}} + u_{R_{\mathrm{P}}} + \sum_{i=1}^{n} u_{M_{\mathrm{P1S}i}} \tag{4}$$

$$\begin{cases} u_{C_{\mathrm{P}}} = \frac{1}{C_{\mathrm{P}}} \int_0^t i_{i_{\mathrm{ref}}}(s)\mathrm{d}s \\ u_{L_{\mathrm{P}}} = L_{\mathrm{P}} \frac{\mathrm{d}i_{\mathrm{ref}}}{\mathrm{d}t} \\ u_{M_{\mathrm{P1S}i}} = M_{\mathrm{P1S}i} \frac{\mathrm{d}i_{\mathrm{S}i}}{\mathrm{d}t} \end{cases}. \tag{5}$$

In the actual system, when the circuit parameters are determined, the parameters in the i_{ref} are also determined. When the absolute value of u_{P} is higher than U_{d}, U_{d} cannot meet the demand of u_{P}, which will force i_{P} waveform distortion and i_{P} cannot track i_{ref}. On the contrary, when the absolute value of u_{P} is always less than U_{d}, i_{P} can track the change of i_{ref}, and the system model can be established based on an equivalent current source model whose output is i_{p}.

The derivation of (4) is shown as follows:

$$\frac{\mathrm{d}u_{\mathrm{P}}}{\mathrm{d}t} = \frac{1}{C_{\mathrm{P}}} i_{\mathrm{ref}} + L_{\mathrm{P}} \frac{\mathrm{d}^2 i_{\mathrm{ref}}}{\mathrm{d}t^2} + R_{\mathrm{P}} \frac{\mathrm{d}i_{\mathrm{ref}}}{\mathrm{d}t} + \sum_{i=1}^{n} M_{\mathrm{P1S}i} \frac{\mathrm{d}^2 i_{\mathrm{S}i}}{\mathrm{d}t^2}. \tag{6}$$

Let (6) be 0 to get k extreme points of the function, denoted t_j ($j = 1, 2, \ldots, k$), then

$$U_{\max} = \max\left\{ |u_{\mathrm{p}}(t_j)|_{j=1,2,\ldots n} \right\} < U_{\mathrm{d}}. \tag{7}$$

If the condition shown in (7) is met, the i_{P} can track the i_{ref}, and the system model can be transformed from based on a voltage source to an equivalent current source. Subsequent analyses in this paper are based on the current source equivalence criteria shown in (7) is met, so a system model based on the equivalent current source can be directly established.

B. System Modeling and Efficiency Characteristic Analysis

Taking the dual-frequency dual-load MCR-WPT system as an example, based on the system shown in Fig. 1, the equivalent model of the WPT system based on HC control is established, as shown in Fig. 4.

In order to analyze the characteristics of the dual-frequency dual-load MCR-WPT system under action of current sources with different frequencies, based on the superposition principle, the system model is established respectively in Fig. 5.

When the f_{i} ($i = 1, 2$) frequency power supply acts alone, the expressions of the pick-up circuit impedance are shown

as

$$\begin{cases} Z_{\mathrm{S1}}^{(i)} = R_{\mathrm{S1}} + R_{\mathrm{L1}} + j\omega_i L_{\mathrm{S1}} + \frac{1}{j\omega_i C_{\mathrm{S1}}} \\ Z_{\mathrm{S2}}^{(i)} = R_{\mathrm{S2}} + R_{\mathrm{L2}} + j\omega_i L_{\mathrm{S2}} + \frac{1}{j\omega_i C_{\mathrm{S2}}} \end{cases}. \tag{8}$$

The KVL formulas are written as follows:

$$\begin{cases} j\omega_i M_{\mathrm{P1S1}} \boldsymbol{I}_i + j\omega_i M_{\mathrm{S1S2}} \boldsymbol{I}_{\mathrm{S2}}^{(i)} = Z_{\mathrm{S1}}^{(i)} \boldsymbol{I}_{\mathrm{S1}}^{(i)} \\ j\omega_i M_{\mathrm{P1S2}} \boldsymbol{I}_i + j\omega_i M_{\mathrm{S1S2}} \boldsymbol{I}_{\mathrm{S1}}^{(i)} = Z_{\mathrm{S2}}^{(i)} \boldsymbol{I}_{\mathrm{S2}}^{(i)} \end{cases}. \tag{9}$$

By substituting (8) into (9), the pick-up circuit current can be solved as

$$\begin{cases} \boldsymbol{I}_{\mathrm{S1}}^{(i)} = \frac{Z_{\mathrm{S2}}^{(i)}(j\omega_i M_{\mathrm{P1S1}}) + (j\omega_i M_{\mathrm{P1S2}})(j\omega_i M_{\mathrm{S1S2}})}{Z_{\mathrm{S1}}^{(i)} Z_{\mathrm{S2}}^{(i)} - (j\omega_i M_{\mathrm{S1S2}})(j\omega_i M_{\mathrm{S1S2}})} \boldsymbol{I}_i \\ \boldsymbol{I}_{\mathrm{S2}}^{(i)} = \frac{Z_{\mathrm{S1}}^{(i)}(j\omega_i M_{\mathrm{P1S2}}) + (j\omega_i M_{\mathrm{P1S1}})(j\omega_i M_{\mathrm{S1S2}})}{Z_{\mathrm{S1}}^{(i)} Z_{\mathrm{S2}}^{(i)} - (j\omega_i M_{\mathrm{S1S2}})(j\omega_i M_{\mathrm{S1S2}})} \boldsymbol{I}_i \end{cases}. \tag{10}$$

The output power is shown as

$$P_{\mathrm{o}}^{(i)} = \left[\mathrm{Re}\left[\boldsymbol{I}_{\mathrm{S1}}^{(i)}\right]\right]^2 R_{\mathrm{L1}} + \left[\mathrm{Re}\left[\boldsymbol{I}_{\mathrm{S2}}^{(i)}\right]\right]^2 R_{\mathrm{L2}}. \tag{11}$$

The system losses are as follows:

$$P_{\mathrm{loss}}^{(i)} = \left[\mathrm{Re}\left(\boldsymbol{I}_{\mathrm{S1}}^{(i)}\right)\right]^2 R_{\mathrm{S1}} + \left[\mathrm{Re}\left(\boldsymbol{I}_{\mathrm{S2}}^{(i)}\right)\right]^2 R_{\mathrm{S2}} + \left(\boldsymbol{I}_{\mathrm{P}}^{(i)}\right)^2 R_{\mathrm{P}}. \tag{12}$$

The reactive power of the system is shown as

$$Q_{\mathrm{sys}}^{(i)} = \left[\mathrm{Im}\left(\boldsymbol{I}_{\mathrm{p}}^{(i)}\right)\right]^2 \mathrm{Im}\left(Z_{\mathrm{Lp}}^{(i)} + Z_{\mathrm{Cp}}^{(i)} + Z_{\mathrm{eq}}^{(i)}\right). \tag{13}$$

The system output power P_{o} and loss P_{loss} are shown as

$$\begin{cases} P_{\mathrm{o}} = P_{\mathrm{o}}^{(1)} + P_{\mathrm{o}}^{(2)} \\ P_{\mathrm{loss}} = P_{\mathrm{loss}}^{(1)} + P_{\mathrm{loss}}^{(2)} \end{cases}. \tag{14}$$

The system efficiency is shown as follows:

$$\eta = \frac{P_{\mathrm{o}}}{P_{\mathrm{o}} + P_{\mathrm{loss}}}. \tag{15}$$

It is can be seen that there is a unique mapping relationship between command current and output power, which can be used as the basis for the design of command current.

The reactive power of the system is shown as

$$Q = Q_{\mathrm{sys}}^{(1)} + Q_{\mathrm{sys}}^{(2)}. \tag{16}$$

The system PF is shown as

$$\mathrm{PF} = \frac{P}{\sqrt{P^2 + Q^2}}. \tag{17}$$

If a zero-compensation strategy is adopted, there will be a large amount of inductive reactive power in the multifrequency system, and adding C_{P} to compensate for inductive reactive power can effectively reduce Q.

IV. Design Method of MFML MCR-WPT System Based on HC Control

According to the working mechanism of the system, the parameters to be designed mainly include control parameters and circuit parameters. The control parameters include i_{ref} and h. The design of i_{ref} determines whether the i_{P} can meet the load requirements, and the value of h affects the control effect and switching frequency at the same time. The circuit parameters mainly include the design of C_{P}, which can compensate for the reactive power of the system. Therefore, the design method of MFML MCR-WPT system based on HC control mainly includes the following three aspects: command current design method, HC width design method, and power compensation capacitor design method. Taking a dual-frequency dual-load WPT system as an example, the system parameters design methods are described in detail in this section.

TABLE I
Simulation Parameters of MFML MCR-WPT System

Parameter	Value	Parameter	Value
f_1	20 kHz	f_2	60 kHz
P_{o1}	30 W	P_{o2}	20 W
M_{P1S1}	18.6 μH	M_{P1S2}	18.6 μH
R_{L1}	3 Ω	R_{L2}	3 Ω
R_{S2}	0.2 Ω	R_{S2}	0.2 Ω

A. Command Current Design Method

According to the working mechanism of the system shown in Fig. 1, the core idea of the design of i_{ref} can be summarized as follows. First, the frequency and amplitude parameters of the corresponding subcommand current are designed according to the frequency and power requirements of each load. Then, the optimization model is established and solved from two aspects of system energy and command current change rate, and the subcommand current phase parameters are obtained. Finally, the subcommand currents are superimposed to form i_{ref}. Detailed command current design steps are shown below.

Step 1: Given the power and frequency requirements of each load, and the other parameters are shown in Table I.

Step 2: f_{i} is set to the working frequency of load;

Step 3: a_{i} is designed according to the mapping relationship between load power and subcommand current amplitude. There is a relationship between a_i and I_i, as shown in the following equation:

$$a_i = \sqrt{2} I_i. \tag{18}$$

For receiving circuits with different resonant frequencies, the cross-coupling between the receiving coils is much smaller than the mutual inductance between the transmitting coil and receiving coils, which can usually be ignored. Therefore, the load currents are shown as

$$\begin{cases} \boldsymbol{I}_{\mathrm{S1}}^{(i)} = \frac{j\omega_i M_{\mathrm{P1S1}}}{Z_{\mathrm{S1}}^{(i)}} \boldsymbol{I}_i \\ \boldsymbol{I}_{\mathrm{S2}}^{(i)} = \frac{j\omega_i M_{\mathrm{P1S2}}}{Z_{\mathrm{S2}}^{(i)}} \boldsymbol{I}_i \end{cases}. \tag{19}$$

The load power expression can be further simplified as

$$\begin{cases} P_{\mathrm{o1}} = \left[\left[\mathrm{Re}\left(\frac{\omega_1 M_{\mathrm{P1S1}}}{Z^{(1)}{}_{\mathrm{S1}}} \boldsymbol{I}_1\right)\right]^2 + \left[\mathrm{Re}\frac{\omega_2 M_{\mathrm{P1S1}}}{Z^{(2)}{}_{\mathrm{S1}}} \boldsymbol{I}_2\right]^2\right] R_{\mathrm{L1}} \\ P_{\mathrm{o2}} = \left[\left[\mathrm{Re}\left(\frac{\omega_1 M_{\mathrm{P1S2}}}{Z^{(1)}{}_{\mathrm{S2}}} \boldsymbol{I}_1\right)\right]^2 + \left(\frac{\omega_2 M_{\mathrm{P1S2}}}{Z^{(2)}{}_{\mathrm{S2}}} \boldsymbol{I}_2\right)^2\right] R_{\mathrm{L2}} \end{cases}. \tag{20}$$

In order to meet the inter-frequency interference suppression criterion [18], the pick-up circuits should maintain a good frequency selection characteristic, then the loop impedance meets

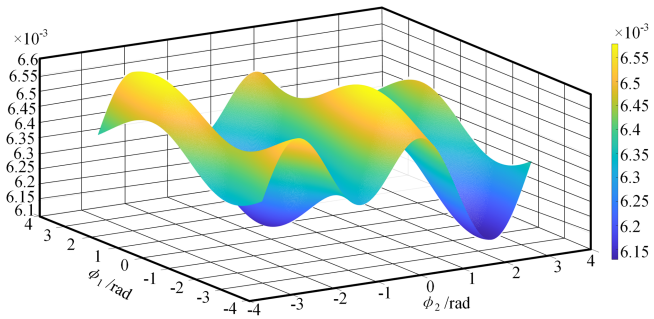

Fig. 6. Change curve of $H(\varphi_1, \varphi_2)$.

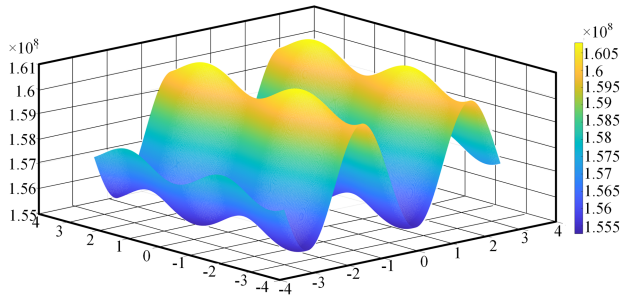

Fig. 7. Change curve of $G(\varphi_1, \varphi_2)$.

the conditions shown as

$$\begin{cases} Z_{\mathrm{S1}}^{(1)} = R_{\mathrm{L1}} + R_{\mathrm{S1}} \\ Z_{\mathrm{S1}}^{(2)} \to \infty \\ Z_{\mathrm{S2}}^{(1)} \to \infty \\ Z_{\mathrm{S2}}^{(2)} \to R_{\mathrm{L2}} + R_{\mathrm{S2}} \end{cases}. \tag{21}$$

Substitute (21) into (20) to further simplify the load power

$$\begin{cases} P_{\mathrm{o1}} = \left(\frac{\omega_1 M_{\mathrm{P1S1}} I_1}{R_{\mathrm{L1}} + R_{\mathrm{S1}}}\right)^2 R_{\mathrm{L1}} \\ P_{\mathrm{o2}} = \left(\frac{\omega_2 M_{\mathrm{P1S2}} I_2}{R_{\mathrm{L2}} + R_{\mathrm{S2}}}\right)^2 R_{\mathrm{L2}} \end{cases}. \tag{22}$$

In combination with (19) and (23), the a_{i} can be obtained by solving the formulas as

$$a_i = \frac{R_{\mathrm{L}i} + R_{\mathrm{S}i}}{2\pi f_i M_{\mathrm{PS}i}} \cdot \sqrt{\frac{2P_{\mathrm{o}i}}{R_{\mathrm{L}i}}}. \tag{23}$$

Step 4: The objective functions of inverter output energy and command current change rate are established, respectively.

1) Energy Equivalent Model: Combined with the dual-frequency dual-load WPT system model shown in Fig. 4, the mathematical model $h(\varphi_1, \varphi_2)$ between the output energy of the inverter in one cycle and phase of subcommand currents is established

$$h(\varphi_1, \varphi_2) = \int_0^{\mathrm{T}} [i_{\mathrm{ref}}(t)]^2 \cdot \mathrm{Re}[Z_{\mathrm{in}}] \mathrm{d}t \tag{24}$$

where Z_{in} is the input impedance of the system.

It can be seen that the system energy $h(\varphi_1, \varphi_2)$ in a period is related to the φ_1 and φ_2, and Z_{in} is a constant when the system circuit parameters are determined, so the model can be further simplified as

$$H(\varphi_1, \varphi_2) = \int_0^{\mathrm{T}} [i_{\mathrm{ref}}(t)]^2 \mathrm{d}t. \tag{25}$$

The variation curve is shown in Fig. 6.

As can be seen from Fig. 6, under the premise that the load power requirements have been met, the values of $H(\varphi_1, \varphi_2)$ are also different as φ_1 and φ_2 form different phase combinations, and in the process of change, there is a combination of φ_1 and φ_2 to make $H(\varphi_1, \varphi_2)$ obtain the minimum value, and the system energy is also the lowest. Therefore, the energy efficiency of the system can be further improved through the phase design.

2) Command Current Rate of Change Model: According to the introduction of the HC control in Section II, the command current change rate will affect the tracking control accuracy when the sampling frequency and accuracy of the system are limited, so reducing the instantaneous command current change rate is helpful to improve the control stability of the system. Therefore, the sum of the instantaneous current change rate of φ_1 and φ_2 in a period is established as

$$g(\varphi_1, \varphi_2) = \int_0^{\mathrm{T}} \left| \frac{\mathrm{d}}{\mathrm{d}t} i_{\mathrm{ref}}(t) \right| dt. \tag{26}$$

In order to facilitate calculation, the model can be further simplified

$$G(\varphi_1, \varphi_2) = \int_0^{\mathrm{T}} \left[\frac{\mathrm{d}}{\mathrm{d}t} i_{\mathrm{ref}}(t) \right]^2 \mathrm{d}t. \tag{27}$$

According to the parameters in Table I, the change curve of $G(\varphi_1, \varphi_2)$ is shown in Fig. 7.

It can be seen from Fig. 7 that under the premise of meeting the load demand, the value of $G(\varphi_1, \varphi_2)$ are different with the different phase combinations, and the influence of φ_1 and φ_2 on $G(\varphi_1, \varphi_2)$ is also different. The combination of φ_1 and φ_2 makes $G(\varphi_1, \varphi_2)$ take the minimum value, and the current change rate of the system in a period is the lowest. Therefore, the control stability of the system can be further improved by adjusting the phase of i_{ref}.

3) Biobjective Optimization: According to the above-mentioned analysis, the optimization model as shown in the formula is established

$$\min F_{R^n}(\varphi_1, \varphi_2) = \min[G(\varphi_1, \varphi_2), H(\varphi_1, \varphi_2)] \tag{28}$$

$$\text{s.t.} \begin{cases} f_1 \neq f_2, \\ \varphi_1, \varphi_2 \in [0, 2\pi], \\ \max |u_{\mathrm{P}}| < U_{\mathrm{d}}. \end{cases} \tag{29}$$

NSGA-II, as a typical representative of multiobjective optimization algorithms, introduces a fast nondominated sorting, and congestion operator to reduce algorithm complexity and better retain excellent individuals [23]. Therefore, this algorithm is chosen in this article to solve the model.

The initial population size is set to 50, and after 1000 iterations, the Pareto frontier nondominated solution set shown in Fig. 8 is generated. The optimized Pareto frontier contains 50 groups of optimal solutions. After weighing the values of the two

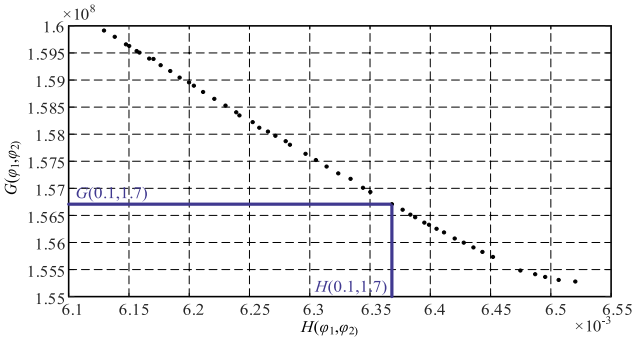

Fig. 8. Pareto frontier nondomination solution set.

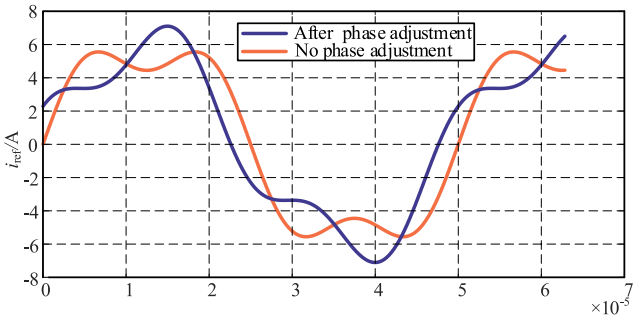

Fig. 9. i_{ref} comparison before and after phase adjustment.

objective functions, the parameters marked in blue in the solution set in Fig. 8 are selected as the optimization result. The objective function values at this point are 6.37×10^{-3} and 1.567×10^{8}, respectively, and the objective functions are both locally optimal. The performance of the system is further improved, and the solution of the model is set as a phase parameter.

Fig. 9 shows the comparison of i_{ref} before and after phase adjustment. Compared with the command current before adjustment, although the peak value of the command current after phase adjustment is increased, the interval between the poles is larger. According to the characteristics of HC control, the actual current change rate at the command current pole is highest, and the current change rate is very high if the command current pole interval is too close, which easily leads to poor control effects. Therefore, under the same hardware condition, the command current after phase adjustment can obtain a better tracking effect.

Step 5: In the actual use process, subcommand currents are calculated offline or online in the primary controller after the load requirements are sent to the primary controller by communication technology. Then the signal generator is used to output subcommand currents directly or the primary controller drives the D/A chip to output the subcommand currents. Finally, the i_{ref} is formed by superimposing the subcommand currents through the adder circuit. Fig. 10 shows the structure of the adder circuit.

$$u_{\mathrm{C}} = -\left(\frac{R_{\mathrm{f}}}{R_{\mathrm{A}}}u_{\mathrm{A}} + \frac{R_{\mathrm{f}}}{R_{\mathrm{B}}}u_{\mathrm{B}}\right). \tag{30}$$

As shown in (30), the superposition output of u_{A} and u_{B} can be realized by adjusting the resistance in the adder circuit.

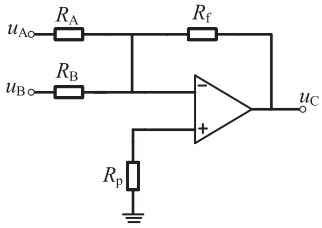

Fig. 10. Schematic diagram of adder circuit.

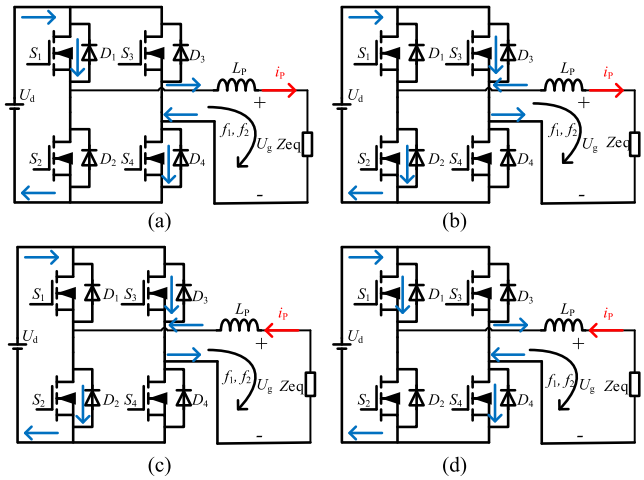

Fig. 11. Circuit mode based on HC control. (a) Circuit mode1. (b) Circuit mode 2. (c) Circuit mode 3. (d) Circuit mode 4.

Therefore, subcommand currents can be superimposed into the desired i_{ref} through the adder circuit.

B. HC Width Design Method

The switching frequency of the inverter based on HC control is not fixed and high, and the selection of h has a great influence on the switching frequency. Therefore, it is necessary to analyze the characteristics of switching frequency under this control mode to guide the design of h. The circuit state based on HC control is shown in Fig. 11.

u_{g} is the equivalent voltage of the system and Z_{eq} is the equivalent impedance of the circuit.

Circuit mode 1,2 is like mode 3,4, except that the current direction in the circuit is different. Therefore, state 1,2 is taken as an example for analysis.

Circuit mode 1: inverter output voltage and circuit current direction are the same, and inductor current increases. The KVL voltage formula according to the current circuit state column is shown as

$$L_{\mathrm{P}}\frac{\mathrm{d}i_{\mathrm{P}}}{\mathrm{d}t} = U_{\mathrm{d}} - u_{\mathrm{g}}. \tag{31}$$

Suppose the circuit state duration is t_1, the switching frequency is very high, and the current change is $2h$ in the period t_1, (31) can be further simplified as

$$t_1 = \frac{2L_{\mathrm{P}}h}{U_{\mathrm{d}} - u_{\mathrm{g}}}. \tag{32}$$

Circuit mode 2: inverter output voltage is opposite to the current in the circuit, and the inductor current is reduced. The KVL voltage formula according to the current circuit state column is shown as

$$L_{\mathrm{P}}\frac{\mathrm{d}i_{\mathrm{P}}}{\mathrm{d}t}=-U_{\mathrm{d}}-u_{\mathrm{g}}. \tag{33}$$

Let the circuit state duration be t_2, similarly, the current change is $2h$ during the t_2 period, and (31) can be derived as

$$t_2=\frac{2L_{\mathrm{P}}h}{U_{\mathrm{d}}+u_{\mathrm{g}}}. \tag{34}$$

The switching frequency is shown as

$$f_{\mathrm{s}}=\frac{1}{t_1+t_2}=\frac{U_{\mathrm{d}}^2-u_{\mathrm{g}}^2}{4L_{\mathrm{P}}U_{\mathrm{d}}h}. \tag{35}$$

When the system current contains two frequency components, u_{g} is shown as

$$u_{\mathrm{g}}=E_1\sin(\omega_1 t+\theta_1)+E_2\sin(\omega_2 t+\theta_2) \tag{36}$$

where E_1 and E_2 are electromotive forces of different frequency components, and θ_1 and θ_2 are voltage phases at different frequencies respectively. There is a relationship between U_{d} and u_{g} as shown in the following equation:

$$\begin{cases}E_1=\lambda_1 U_{\mathrm{d}}\\ E_2=\lambda_2 U_{\mathrm{d}}\end{cases} \tag{37}$$

where $0\le\lambda_1,\lambda_2\le 1$.

The instantaneous switching frequency f_{s} expression can be further derived as

$$f_s=\underbrace{\frac{U_{\mathrm{d}}}{4L_{\mathrm{P}}h}\left(1-\frac{\lambda_1^2+\lambda_2^2}{2}\right)}_{\text{Average switching frequency}}+\underbrace{\begin{array}{l}\frac{U_{\mathrm{d}}}{8L_{\mathrm{P}}h}[\lambda_1^2\cos(2\omega_1 t+\theta_1)+\lambda_2^2\cos 2(\omega_2 t+\theta_2)\\ -4\lambda_1\lambda_2\sin(\omega_1 t+\theta_1)\sin(\omega_2 t+\theta_2)]\end{array}}_{\text{Fluctuating switching frequency}}. \tag{38}$$

As can be seen from (38), the switching frequency of the inverter is not a fixed value and can be divided into average switching frequency and fluctuating switching frequency. In terms of switching loss, it is mainly determined by the average switching frequency, while fluctuating switching frequency affects the upper and lower thresholds of switching frequency. It can be seen from (35) that the maximum switching frequency during operation is shown in the following equation:

$$f_{s\max}=\frac{U_{\mathrm{d}}}{4L_{\mathrm{P}}h}. \tag{39}$$

It can be seen from (39) that the maximum switching frequency of the system is affected by U_{d}, L_{P}, and h, while the real-time switching frequency is also related to the load state of the secondary side. With the increase of sampling frequency, the inverter switching frequency will be more consistent with the theoretical switching frequency, and will not exceed f_{smax}. Therefore, the sampling frequency of i_{P} should be increased as much as possible to obtain a good current tracking effect.

According to the principle of HC control, i_{p} always changes with i_{ref} within h. So, the maximum current change within a switching cycle is $2h$, and the maximum current ripple is $2h$. The ratio between the maximum ripple current value and the absolute value of i_{ref} is defined as σ, as shown in the following equation:

$$\sigma=\frac{\Delta i_{\mathrm{P}\max}}{|i_{\mathrm{ref}}|}=\frac{2h}{|i_{\mathrm{ref}}|} \tag{40}$$

where σ is proportional to h and inversely proportional to the absolute value of i_{ref}. If σ is smaller, i_{p} waveform is smoother, and current tracking effect is better. However, the decrease of σ will also lead to the increase in f_{smax}. In the application process, the selection of h should fully consider the bearing capacity of the switching device, the current tracking effect, and the processing speed of the controller. A small h should be selected as far as possible under the premise of ensuring the safety of the device to obtain a better current tracking effect.

C. Design Method of Power Compensation Capacitor

According to the analysis in Section III, for an MFML MCR-WPT system, there are large amount of multifrequency power in the system at the same time, and if power quality management is not carried out, there will be a large amount of reactive power in the system, which will decrease PF. The reactive power compensation of the MFML MCR-WPT systems with voltage superposition technologies requires a multifrequency resonant network, which has high design complexity. However, the current output of the system based on HC control is only controlled by i_{ref}, and adding C_{P} will not affect the main frequency component of the output current. Therefore, reactive power can be compensated by adding C_{P} in a way with low cost and design complexity. The parameter design process includes the following steps.

According to the system circuit model shown in Fig. 4, when the power supply with operating frequency f_{i} acts, the reactive power gap in the system is shown in the following equation:

$$\Delta Q^{(i)}=I_i^2\cdot\mathrm{Im}\left(Z_{L\mathrm{P}}^{(i)}+Z_{\mathrm{eqS1}}^{(i)}+Z_{\mathrm{eqS2}}^{(i)}\right). \tag{41}$$

The expression of the capacitive reactive power generated by C_{P} is shown in the following equation:

$$Q_{C_{\mathrm{P}}}^{(i)}=\frac{I_i^2}{\omega_i C_{\mathrm{P}}}. \tag{42}$$

The total reactive power gap of the dual-frequency dual-load WPT system is shown in the following equation:

$$\Delta Q=\Delta Q^{(1)}+\Delta Q^{(2)}. \tag{43}$$

The expression of total capacitive reactive power emitted by C_{P} at multiple frequencies is shown in the following equation:

$$Q_{C_{\mathrm{P}}}=Q_{C_{\mathrm{P}}}^{(1)}+Q_{C_{\mathrm{P}}}^{(2)}. \tag{44}$$

The reactive power gap of the system is compensated from the perspective of the overall reactive power balance of the system while maintaining the weak inductivity of the system, C_{P} can

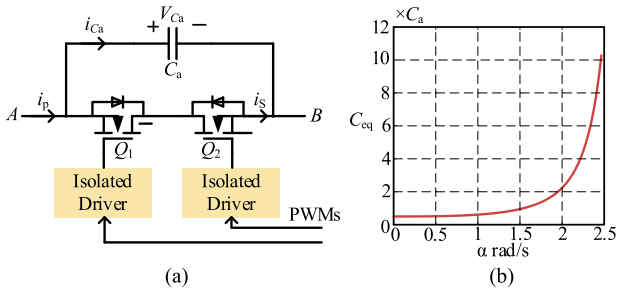

Fig. 12. Structure of the SCC and the relation between the α and C_{eq}. (a) Structure of SCC. (b) Relation between α and C_{eq}.

be obtained as shown in the following equation:

$$C_P = (0.9 - 0.95) \cdot \frac{\sum_{i=1}^{n} \frac{I_i^2}{\omega_i}}{\Delta Q}. \tag{45}$$

To ensure that the system always maintains a high PF when the load changes, the C_P value can be changed by a capacitance matrix or switch-controlled capacitor (SCC) [24].

Where α is the on-angle of the switching tube, and C_{eq} is the equivalent capacitance between A and B.

The basic unit of SCC is shown in Fig. 12(a). A fixed-value capacitor C_a is connected in parallel with two switching tubes to form a basic SCC. C_{eq} can be changed by controlling α, and the relationship between α and C_{eq} is shown in the following equation:

$$C_{eq} = \frac{C_a}{2 - (2\alpha - \sin(2\alpha))/\pi}. \tag{46}$$

Fig. 12(b) shows the relationship between C_{eq} and α. C_{eq} can be equivalent to different capacitance values as α changes. Therefore, according to different load requirements, combined with (46) to solve α, to achieve the increase of PF when the load demands change.

V. Simulation and Experimental Verification

To verify the correctness of the theory proposed in this article, we built the experimental device as shown in Fig. 13.

The inverter is designed based on a GAN device, which has the characteristics of high switching frequency and low switching loss. The control module includes an HC control circuit and dead zone circuit. The operational amplifier of HC control circuit uses AD826 of Analog Devices, and the voltage comparator uses AD790, which can realize fast voltage comparison and has a built-in hysteresis function, which can minimize the oscillation of the comparator output when the comparator input voltage is close to the comparison threshold, contributing to the stable output of the switching signal. R/S flip-flop is composed of SN74HC132 of Texas Instruments, which is quadruple 2-Input NAND Gates with Schmitt-Trigger inputs. The dead zone of the switching signal is generated by the dead zone circuit, and the dead zone time is set to 150 ns. Current sampling adopts MCA1101 series current sensor of Aceinna, which supports

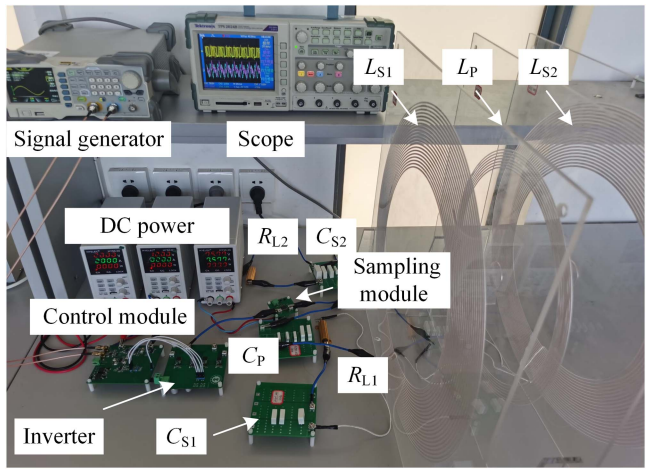

Fig. 13. Dual-frequency dual-load WPT experimental device based on HC control.

TABLE II
System Parameters

Parameter	Value	Parameter	Value
L_P	34.58 μH	R_P	0.092 Ω
L_{S1}	233.5 μH	R_{S1}	0.2 Ω
L_{S2}	233.28 μH	R_{S2}	0.24 Ω
M_{P1S1}	18.019 μH	M_{P1S2}	11.52 μH
R_{L1}	1–10 Ω	R_{L2}	1–10 Ω
C_{S1}(20 kHz Channel)	271.05 nF	C_{S1}(30 kHzChannel)	120.52 nF
C_{S2}	30.16 nF		

current bandwidth up to 1.5 MHz. Other parameters of the experimental device are shown in Table II.

A. Verification of Equivalent Current Source Characteristics

The equivalent current source characteristics of the MCR-WPT system based on HC control mainly include the following two aspects. First, under the condition that the remaining circuit parameters are determined, if U_d is higher than the equivalent voltage threshold U_{max}, i_P can track i_{ref}. On the contrary, if U_d is lower than U_{max}, the i_P is distorted and cannot change with i_{ref}. Second, under the condition that the system parameters meet the equivalent current source criterion, i_P is only controlled by i_{ref}, and the inverter can output the current of any frequency, and switch power frequency freely.

According to the equivalent current source criterion, when the U_d does not reach the threshold voltage, it will be difficult for i_P to effectively track the i_{ref}. Set $i_{ref} = 2\sin(20\,000t)$, and according to the current source equivalence criterion, the U_{max} is 10.08 V. In order to ensure that the inverter switching frequency is within the allowable range of the switching device, h is selected as 0.3. As shown in Fig. 14, when U_d is set to 7 V, the current source equivalence criterion is not met, the i_P waveform is distorted, and it is difficult to track i_{ref}. After t_s, the i_{ref} can be tracked i_P within h. From the waveform of u_{in}, the inverter switching frequency is not fixed, which is consistent with the typical characteristics of HC control.

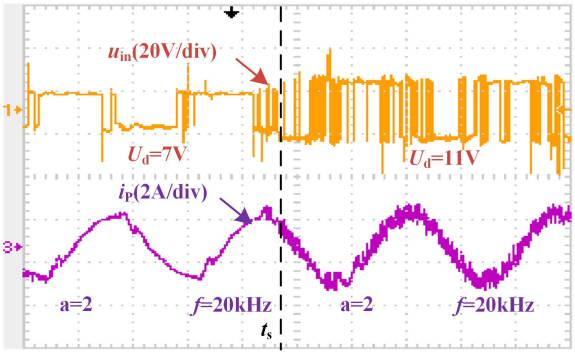

Fig. 14. Experimental waveform of u_{in} and i_P when U_d is switched at t_s.

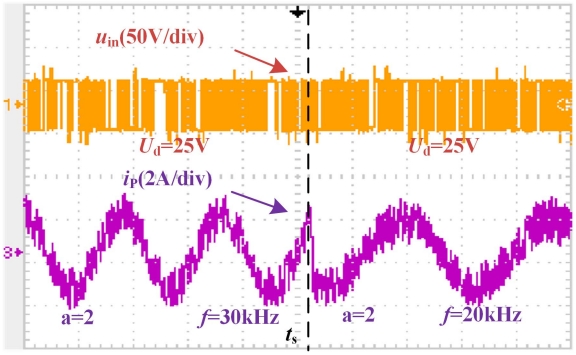

Fig. 15. Experimental waveform of u_{in} and i_P when i_{ref} frequency is switched at t_s.

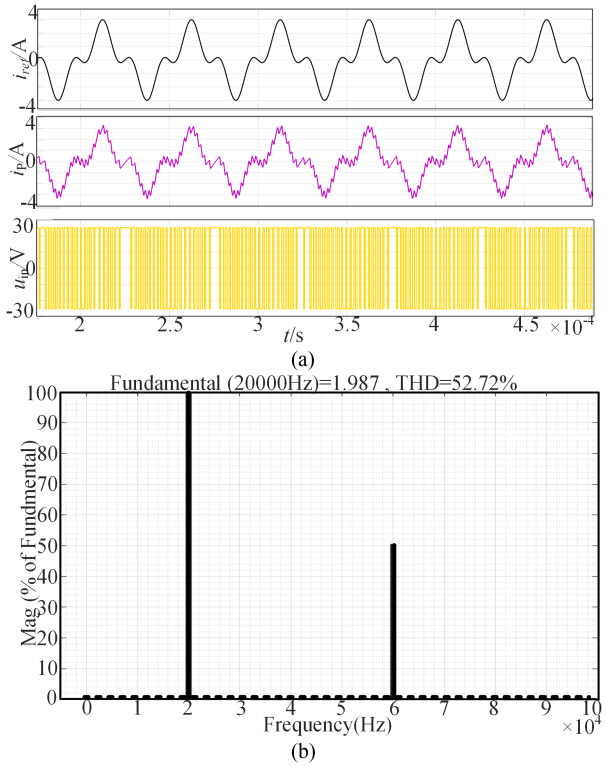

Fig. 16. System simulation waveform and the FFT analysis result of i_P. (a) Simulation waveform of i_{ref}, i_P, and u_{in}. (b) FFT analysis result of i_P which fundamental is 20 kHz.

Under the condition that the equivalent current source criterion is met, the circuit structure is not changed, and the i_{ref} frequency is switched from 20 to 30 kHz at t_s. The u_{in} and i_P waveforms are shown in Fig. 15. The inverter can switch the current between different frequencies with rapid response freely. It is shown that the external circuit topology does not affect i_P under the condition that the equivalent current source criterion is met, so the system model be established based on the equivalent current source model, and it is also proved that adding C_P can directly compensate the reactive power without affecting the inverter output current.

B. System Multifrequency Output Characteristic Verification

In order to verify the multifrequency output characteristics of the system based on HC control, the dual-frequency dual-load is taken as an example to control the inverter to output the dual-frequency current of 20 and 60 kHz superposition at the same time. According to the i_{ref} design steps described above, set $i_{ref} = 2\sin(20\,000t + 0.1) + \sin(60\,000t + 1.58)$. Ensure that the switching frequency of the switching devices is within the allowable range of the switching device, h is set to 0.3, and the equivalent current source criterion is met, then U_d is set to 25 V, R_{L1} is set to 1 Ω and R_{L2} is set to 3 Ω.

Fig. 16 shows the system simulation waveform obtained by building a simulation model according to the above-mentioned parameters. It can be seen from Fig. 16(a) that i_{ref} is tracked by i_P within h, and the frequency of u_{in} also changes with the current. From the FFT analysis result of i_P as shown in Fig. 16(b), i_P mainly contains 20 and 60 kHz frequency components.

Fig. 17 shows the simulation waveform and FFT analysis results of the load current. From the current waveform, the load can achieve stable reception of the corresponding frequency current, and from the FFT analysis results of the load current, there are almost no other frequency components in the load current, and the load current are standard sine wives.

Fig. 18 shows the system output experimental waveform with the same parameters. By comparing the experimental waveform with the simulation waveform, it can be found that they are basically consistent, indicating that the multifrequency power output can be realized based on the theory proposed in this article.

Similarly, change the frequency composition of i_{ref}, let the inverter output 30 and 60 kHz superposition current. Set $i_{ref} = 2\sin(30\,000t + 0.2) + \sin(60\,000t + 1.9)$, $R_{L1} = 1\ \Omega$, $R_{L2} = 3\ \Omega$ $h = 0.3$, $U_d = 25$ V, the load current simulation and experimental waveform are shown in Fig. 19. The load can receive sinusoidal current of corresponding frequency, and the experimental current is basically consistent with the simulation current waveform, indicating that the proposed method can realize flexible switching of output current frequency under multiload condition.

To verify that decoupling control can be achieved between different frequency powers, Fig. 20 shows the load current experiment waveforms of 60 kHz frequency power added at t_s during 20 kHz power transmission. When the inverter output

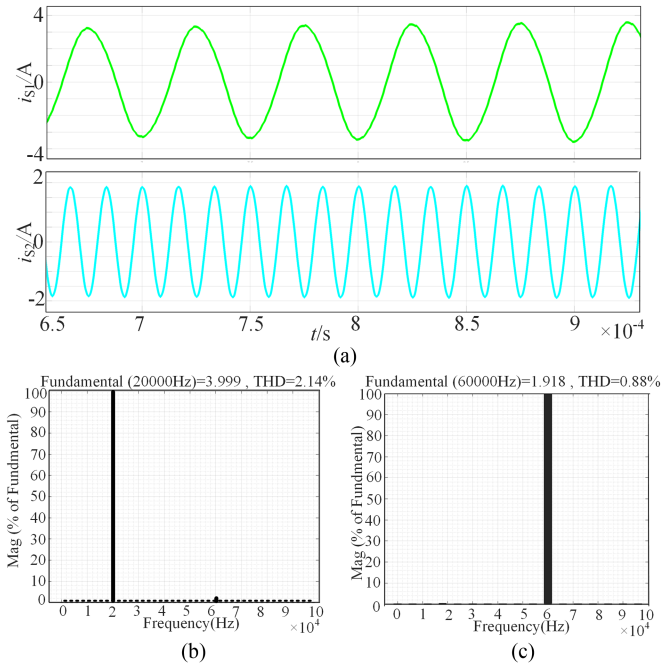

Fig. 17. Load current simulation waveform and the FFT analysis results. (a) Simulation waveform of i_{s1}, i_{s2}. (b) FFT analysis result of i_{s1}. (c) FFT analysis result of i_{s2}.

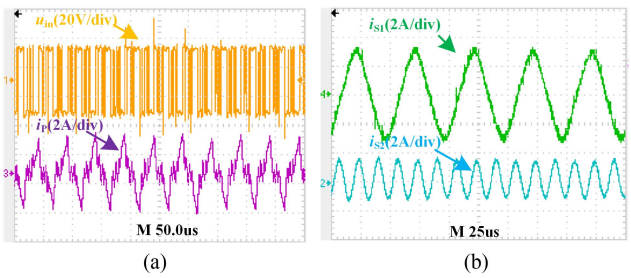

Fig. 18. System experimental waveform when 20 and 60 kHz frequency components are superimposed (a). u_{in} and i_{P} waveform. (b) i_{S1} and i_{S2} waveform.

current is added to the 60 kHz frequency current at t_{s}, the 20 kHz frequency channel can still maintain stable power reception, and the load of 60 kHz frequency channel can also receive corresponding frequency power.

As shown in Fig. 21, before t_{s}, the inverter outputs 20 and 60 kHz currents at the same time, and the amplitude of the subcommand current corresponding to the 20 kHz current is reduced to 2/3 of the original value at t_{s}. The amplitude of i_{S1} drops to 2/3 of that before switching, while the amplitude of i_{S2} does not change, which indicates that the WPT system based on HC control can realize the decoupling transmission of power between different frequencies.

According to the principle of HC control, when the command current does not change, the inverter output current is constant. Consequently, the MFML MCR-WPT system based on HC control can keep the primary current and the secondary induced voltage constant. Because the coil in the actual system is not

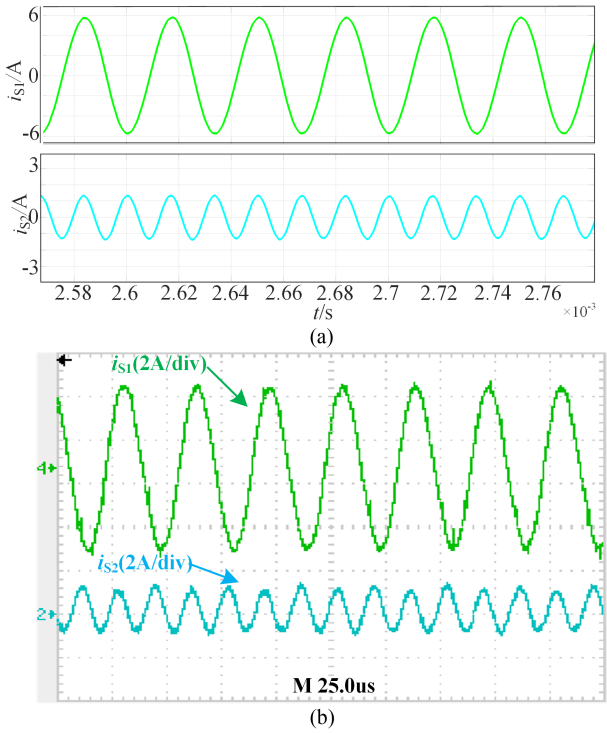

Fig. 19. Load current simulation and experimental waveform when 30 and 60 kHz frequency components are superposed. (a) Simulation waveform. (b) Experimental waveform.

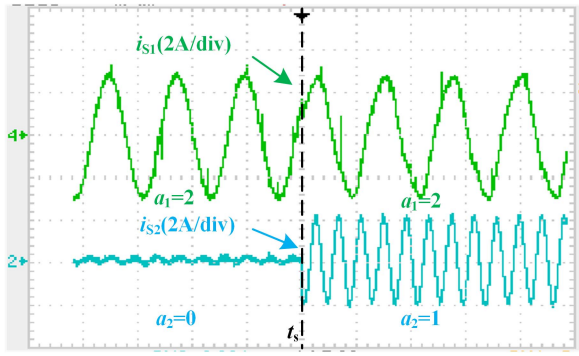

Fig. 20. Load current experiment waveforms of 60 kHz frequency power is added at t_{s} during 20 kHz power transfer.

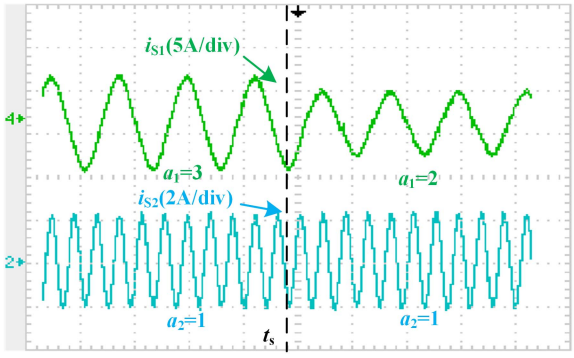

Fig. 21. Load current experimental waveforms when a_1 is switched at t_{s}.

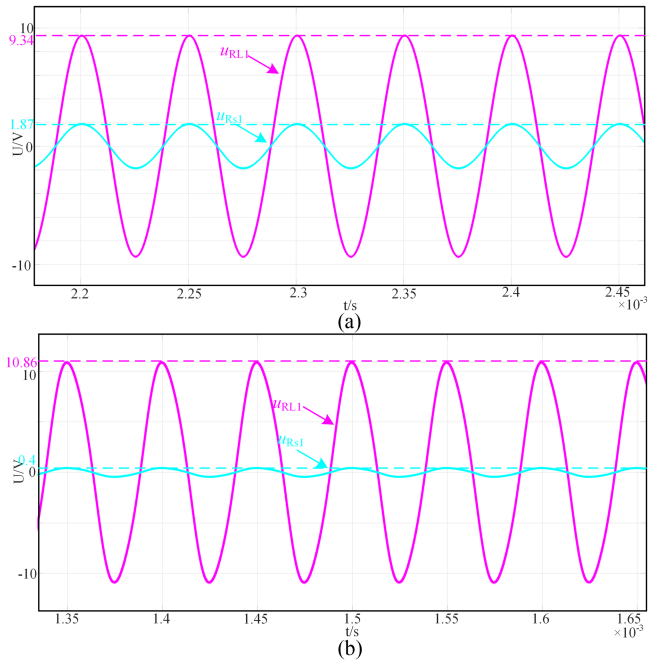

Fig. 22. Simulation waveform of u_{RL1} and u_{RS1}. (a) Waveform of u_{RL1} and u_{RS1} when $R_{L1} = 1\ \Omega$. (b) Waveform of u_{RL1} and u_{RS1} when $R_{L1} = 5\ \Omega$.

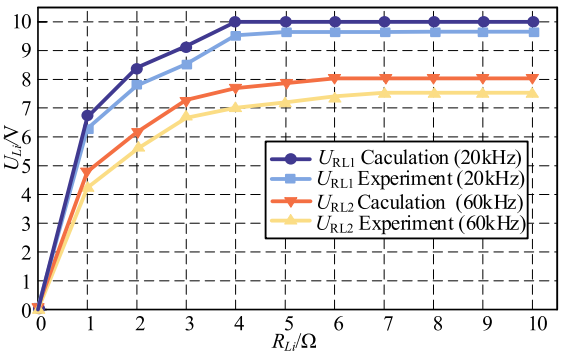

Fig. 23. Load voltage variation curve with the same i_P.

a pure inductance, it is composed of equivalent resistance and inductance. The equivalent resistance relates to the load in series and has a voltage division effect on the load voltage. Taking the 20 kHz channel as an example, a_1 is set to 5 A, the peak of secondary induced voltage u_{out1} is 11.32 V. As shown in Fig. 22. When $R_{L1} = 1\ \Omega$, the voltage division of R_{S1} cannot be ignored, resulting in a large difference between u_{RL1} and u_{out1}. The peak voltage after adding u_{RS1} is 11.21 V, which is almost the same as u_{out1}. When $R_{L1} = 5\ \Omega$, the peak voltage on R_{S1} is only 0.4 V, and the peak after adding u_{RL1} is 11.26 V, which is almost the same as u_{out1}.

As shown in Fig. 23, when R_{Li} ($i = 1, 2$) is small, the R_{si} is relatively close to R_{Li}, and the voltage division effect of R_{si} is obvious, which leads to a large gap between u_{RLi} and u_{outi}. With the increase of R_{Li}, the voltage division effect of R_{si} has less influence on u_{RLi}, so u_{RLi} gradually approaches u_{outi}, which can achieve constant voltage output on the secondary side.

Since the secondary side of the proposed system can be equivalent to a constant voltage source, short circuits on the load side should be avoided as much as possible in the actual system. Because it may cause the inverter dc power supply to output too much power and damage the system. Although the system based on HC control has the current limiting characteristic, it has a protective effect on this situation, but short circuits on the load side should be avoided as much as possible.

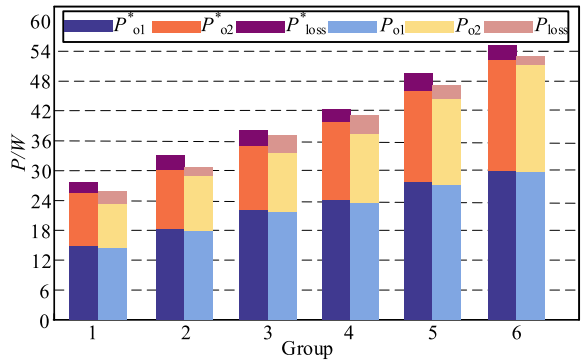

Fig. 24. System load power comparison diagram with different design power values.

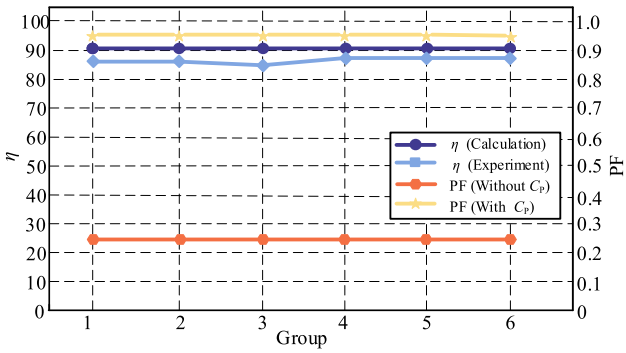

Fig. 25. Calculation and experimental transfer efficiency curves and PF comparison curves.

Where P^*_{o1}, P^*_{o2}, P^*_{loss} are calculation value, and P_{o1}, P_{o2}, P_{loss} are experimental value.

Set $R_{L1} = R_{L2} = 5\ \Omega$, the comparison diagram between the experimental load power and the calculation power of the system at different design values is shown in Fig. 24. The experimental load power can basically reach the design power value. Because the load voltage is slightly lower than the theoretical voltage, the experimental power of the system is slightly lower than the calculation value, but these differences are so small that they are considered negligible.

In this article, inverter loss is not considered when calculating system efficiency, and only transfer efficiency is calculated. As can be seen from Fig. 25, the change trend of the experimental value of the system transfer efficiency is the same as that of the calculation value, but the experimental value is slightly lower than the calculation efficiency due to the instrument measurement error. The PF of the system without C_P is all lower than 0.3, after C_P is added, the PF increases more than 0.9, indicating that the MFML MCR-WPT system based on HC control can raise PF without affecting the power transmission.

TABLE III
COMPARISON OF DIFFERENT MFML MCR-WPT TECHNOLOGIES

	η(%)	Transmission mechanism	Power output mode	Independent power control	Compensation mode
[10]	75	Multiple-inverter parallel operation	Parallel output	Yes	zero-compensation
[14]	70–80	Fundamental-harmonic reuse	Parallel output	No	MFRC network
[15]	24–29	Time-sharing	Time-sharing	Yes	Resonance compensation
[18]	65–70	HMW-SPWM	Parallel output	Yes	zero-compensation
Proposed	80–90	HC Control	Parallel output	Yes	compensating capacitance

C. Comparative Analysis of Existing MFML MCR-WPT Technologies

According to the classification of existing MFML MCR-WPT technologies in Section I, a representative paper in each category of technologies is selected and compared with the proposed system.

In Table III, the existing technologies are compared from five aspects: efficiency, transmission mechanism, power output mode, independent power control, and compensation mode.

In [10], multiple inverters are controlled in parallel operation to output multifrequency power and decoupling control of each frequency component, but it brings a larger system volume. In [14], the fundamental harmonic reuse technology is adopted to output multifrequency power by controlling the frequency component in the output voltage of the inverter, and the MFRC network is adopted to make the system work in a resonant state. However, this technology requires a large amount of off-line calculation when calculating the switch angle, which is not conducive to closed-loop regulation. At the same time, the structure and design complexity of the MFRC network increases greatly when the number of loads is increased. In [15], the idea of time-sharing is used to output power of different frequencies at different times, but it is difficult to achieve parallel output of multifrequency power, and the system needs to be retuned when switching the frequency of power. In [18], HMW-SPWM is adopted to realize parallel transmission and decoupling control of multifrequency power, but the zero-compensation strategy is adopted on the primary side, resulting in more reactive power in the system.

Compared with the above-mentioned technologies, the proposed system realizes the parallel transmission and decoupling control of multifrequency power, and adopts compensation capacitor to keep the high PF of the system. Compared with the system using a zero-compensation strategy, the system PF is higher. Compared with the system using the MFRC network, the proposed system compensation structure and design method are simpler, and there is no need to change the circuit structure as the number of loads increases, and the design complexity changes little.

VI. CONCLUSION

This article presents an MFML MCR-WPT system based on HC control. First, the structure and working mechanism of the system are introduced in detail, which outputs multifrequency power by tracking the command current, which consists of subcommand currents designed according to different load requirements. Second, the condition that the system can realize current tracking is analyzed. Based on this condition, the system model is established and its characteristics are analyzed. Then, this article gives detailed parameter design methods, including the command current design method, HC width design method, and power compensation capacitor design method. Finally, the correctness of the proposed technology is verified by simulation and experiment results.

However, the proposed system still has some shortcomings, which need to be further studied in the future.

1) Only the power supply demand of ac loads is analyzed, however, the research on dc loads and its voltage regulation strategy is insufficient. Therefore, the closed-loop voltage regulation strategies should be studied for different loads to dynamically meet the needs of loads in the future.
2) To achieve better tracking performance, the inverter in the MCR-WPT system based on HC control must maintain a high switching frequency, which increases switching losses. So, the methods to reduce switching losses should be studied to further improve the efficiency of the system.

REFERENCES

[1] B. Zhang, X. Shu, and R. Huang, "The development of inductive and resonant wireless power transfer technology," *Trans. China Electrotechn. Soc.*, vol. 32, no. 18, pp. 3–17, Sep. 2017.
[2] A. Sarin and A.-T. Avestruz, "Code division multiple access wireless power transfer for energy sharing in heterogenous robot swarms," *IEEE Access*, vol. 8, pp. 132121–132133, 2020.
[3] H. Yan, Y. Chen, and S. Yang, "UAV-enabled wireless power transfer with base station charging and UAV power consumption," *IEEE Trans. Veh. Technol.*, vol. 69, no. 11, pp. 12883–12896, Nov. 2020.
[4] Y. Zeng et al., "Misalignment insensitive wireless power transfer system using a hybrid transmitter for autonomous underwater vehicles," *IEEE Trans. Ind. Appl.*, vol. 58, no. 1, pp. 1298–1306, Jan./Feb. 2022.
[5] Y. Geng, Z. Yang, and F. Lin, "Design and control for catenary charged light rail vehicle based on wireless power transfer and hybrid energy storage system," *IEEE Trans. Power Electron.*, vol. 35, no. 8, pp. 7894–7903, Aug. 2020.
[6] P. Zhang, S. Maryam, O. C. Onar, Q. Yang, and C. Cai, "A field enhancement integration design featuring misalignment tolerance for wireless EV charging using LCL topology," *IEEE Trans. Power Electron.*, vol. 36, no. 4, pp. 3852–3867, Apr. 2021.
[7] J. Wang et al., "A 403 MHz wireless power transfer system with tuned split-ring loops for implantable medical devices," *IEEE Trans. Antennas Propag.*, vol. 70, no. 2, pp. 1355–1366, Feb. 2022.

[8] C. Luo, D. Qiu, B. Zhang, W. Xiao, and Y. Chen, "Wireless power transfer system for multiple loads," *Trans. China Electrotechn. Soc.*, vol. 35, no. 12, pp. 2549–2516, Jun. 2020.
[9] Y. Wu, S. Zhao, S. Zhang, J. Zhang, and X. Wang, "An adaptive impedance matching method based on radial basis function neural network in Multi-load wireless power transfer systems," *Trans. China Electrotechn. Soc.*, vol. 36, no. 19, pp. 3969–3977, Oct. 2021.
[10] F. Liu, Y. Yang, Z. Ding, X. Chen, and R. M. Kennel, "A multifrequency superposition methodology to achieve high efficiency and targeted power distribution for a multiload MCR WPT system," *IEEE Trans. Power Electron.*, vol. 33, no. 10, pp. 9005–9016, Oct. 2018.
[11] D. Ahn and P. P. Mercier, "Wireless power transfer with concurrent 200-kHz and 6.78-MHz operation in a single-transmitter device," *IEEE Trans. Power Electron.*, vol. 31, no. 7, pp. 5018–5029, Jul. 2016.
[12] C. Xia, S. Ren, N. Ma, Y. Hou, Y. Sun, and J. Chen, "Inductively coupled power transfer system with fundamental wave and harmonic wave two-path parallel transmission," *Autom. Electric Power Syst.*, vol. 41, no. 7, pp. 93–100, Apr. 2017.
[13] C. Zhao and D. Costinett, "GaN-based dual-mode wireless power transfer using multifrequency programmed pulse width modulation," *IEEE Trans. Ind. Electron.*, vol. 64, no. 11, pp. 9165–9176, Nov. 2017.
[14] C. Qi, H. Miao, Z. Lang, and X. Chen, "A generalized methodology to generate, amplify and compensate multi-frequency power for a single-inverter-based MF-MR-S-WPT system," *IEEE Access*, vol. 8, pp. 181513–181525, 2020.
[15] Y.-J. Kim, D. Ha, W. J. Chappell, and P. P. Irazoqui, "Selective wireless power transfer for smart power distribution in a miniature-sized multiple-receiver system," *IEEE Trans. Ind. Electron.*, vol. 63, no. 3, pp. 1853–1862, Mar. 2016.
[16] D. Thenathayalan and J.-H. Park, "Individually regulated multiple-output WPT system with a single PWM and single transformer," *IEEE J. Emerg. Sel. Topics Power Electron.*, vol. 8, no. 4, pp. 3542–3557, Dec. 2020.
[17] D. Thenathayalan and J.-H. Park, "An independently controlled single-PWM multiple-output narrow-band resonant converter," *IEEE Trans. Power Electron.*, vol. 33, no. 6, pp. 5042–5061, Jun. 2018.
[18] C. Xia, N. Wei, H. Zhang, S. Zhao, Z. Li, and Z. Liao, "Multifrequency and multiload MCR-WPT system using hybrid modulation waves SPWM control method," *IEEE Trans. Power Electron.*, vol. 36, no. 11, pp. 12400–12412, Nov. 2021.
[19] Z. Liu, M. Su, Q. Zhu, Y. Chao, S. Zang, and A. P. Hu, "A dual-frequency 3-D WPT system with directional power transfer capability at two separately regulated outputs," *IEEE J. Emerg. Sel. Topics Power Electron.*, vol. 11, no. 3, pp. 2514–2524, Jun. 2023.
[20] Z. Zhang, X. Li, H. Pang, H. Komurcugil, Z. Liang, and R. Kennel, "Multiple-frequency resonating compensation for multichannel transmission of wireless power transfer," *IEEE Trans. Power Electron.*, vol. 36, no. 5, pp. 5169–5180, May 2021,.
[21] S. Samanta and A. K. Rathore, "Wireless power transfer technology using full-bridge current-fed topology for medium power applications," *IET Power Electron.*, vol. 9, no. 9, pp. 1903–1913, Jul. 2016.
[22] C. Anyapo, N. Teerakawanich, C. Mitsantisuk, and K. Ohishi, "Development of wireless power transfer with primary-side current mode control capability using virtual-current source resonant inverter," in *Proc. IEEE 44th Annu. Conf. Ind. Electron. Soc.*, 2018, pp. 4805–4809.
[23] X. Liu, J. Sun, L. Zheng, S. Wang, Y. Liu, and T. Wei, "Parallelization and optimization of NSGA-II on Sunway TaihuLight System," *IEEE Trans. Parallel Distrib. Syst.*, vol. 32, no. 4, pp. 975–987, Apr. 2021.
[24] Z. Hu, Y. Qiu, L. Wang, and Y.-F. Liu, "An interleaved LLC resonant converter operating at constant switching frequency," *IEEE Trans. Power Electron.*, vol. 29, no. 6, pp. 2931–2943, Jun. 2014.

Anran Sun received the B.S. degree in electrical engineering and intelligent control from the School of Electrical and Control Engineering, Liaoning Technical University, Huludao, China, in 2019. He is currently working toward the Ph.D. degree in electrical engineering with the School of Electrical Engineering, China University of Mining and Technology, Xuzhou, China.

His research interest focuses on wireless power transfer.

Chenyang Xia (Member, IEEE) was born in Jiangsu Province, China, in 1982. He received the B.S., M.S., and Ph.D. degrees in control theory and control engineering from the Chongqing University, Chongqing, China, in 2006, 2008, and 2010, respectively.

From 2018 to 2019, he was an Academic Visitor with the University of Auckland, Auckland, New Zealand. He is currently a Professor with the School of Electrical Engineering, China University of Mining and Technology, Xuzhou, China. His research interests include wireless power transfer and intelligent control.

Yuhang Chen received the B.S. degree in electrical engineering in 2022 from the China University of Mining and Technology, Xuzhou, China, where he is currently working toward the M.S. degree in electrical engineering with the School of Electrical Engineering.

His research interest focuses on wireless power transfer.

Yunhai Liu received the B.S. degree in electrical engineering in 2021 from the China University of Mining and Technology, Xuzhou, China, where he is currently working toward the M.S. degree in electrical engineering with the School of Electrical Engineering.

His research interests include wireless power transfer and intelligent control.

Ziyue Yang received the B.S. degree in electrical engineering in 2020 from the China University of Mining and Technology, Xuzhou, China, where he is currently working toward the Ph.D. degree in electrical engineering with the School of Electrical Engineering.

His research interest focuses on wireless power transfer.

Shuze Zhao received the B.S. degree in electrical engineering in 2018 from the China University of Mining and Technology, Xuzhou, China, where he is currently working toward the Ph.D. degree in electrical engineering with the School of Electrical Engineering.

His research interest focuses on wireless power transfer.

Zijian Yang received the B.S. degree in electrical engineering in 2021 from the China University of Mining and Technology, Xuzhou, China, where he is currently working toward the M.S. degree in electrical engineering with the School of Electrical Engineering.

His research interest focuses on wireless power transfer.